Biologically Inspired Artificial Compound Eyes

Ki-Hun Jeong, *et al.*

Science **312**, 557 (2006);
DOI: 10.1126/science.1123053

Science (print ISSN 0036-8075; online ISSN 1095-9203) is published weekly, except the last week in December, by the American Association for the Advancement of Science, 1200 New York Avenue NW, Washington, DC 20005.

Biologically Inspired Artificial Compound Eyes

Ki-Hun Jeong, Jaeyoun Kim, Luke P. Lee*

This work presents the fabrication of biologically inspired artificial compound eyes. The artificial ommatidium, like that of an insect's compound eyes, consists of a refractive polymer microlens, a light-guiding polymer cone, and a self-aligned waveguide to collect light with a small angular acceptance. The ommatidia are omnidirectionally arranged along a hemispherical polymer dome such that they provide a wide field of view similar to that of a natural compound eye. The spherical configuration of the microlenses is accomplished by reconfigurable microtemplating, that is, polymer replication using the deformed elastomer membrane with microlens patterns. The formation of polymer waveguides self-aligned with microlenses is also realized by a self-writing process in a photosensitive polymer resin. The angular acceptance is directly measured by three-dimensional optical sectioning with a confocal microscope, and the detailed optical characteristics are studied in comparison with a natural compound eye.

Compound eyes in nature present intriguing topics in physiological optics because of their unique optical scheme for imaging. For example, a bee's eye has thousands of integrated optical units called ommatidia spherically arranged along a curvilinear surface so that each unit points in a different direction (Fig. 1A). Each ommatidium consists of a light-diffracting facet lens, a crystalline cone, and photoreceptor cells with a wave-guiding rhabdom (*1*–*3*) (Fig. 1B). The omnidirectionally arranged ommatidium collects incident light with a narrow range of angular acceptance and independently contributes to the capability of wide field-of-view (FOV) detection (*4*–*6*).

Artificial implementation of compound eyes has attracted a great deal of research interest, because the wide FOV exhibits a huge potential for medical, industrial, and military applications. So far, imaging with a FOV over 90° has been achieved only with fish eye lenses, which rely on bulky and expensive multiple lenses and require stringent alignment. The use of miniaturized, arrayed optical components fabricated by using semiconductor planar processing technologies has been proposed to simultaneously mimic the structure and function of an individual ommatidium and the large-scale collection of ommatidia. The imaging systems using microlens arrays (*7*, *8*) or graded index rod arrays (*9*, *10*) in combination with matching pinhole arrays are good examples. More biomimetic efforts to implement artificial compound eyes were reviewed in (*11*) along with an outline of biological imaging systems. Achieving a wide FOV in those structures, however, has been hindered mainly by the inherent flatness of the arrayed optical components. In addition, the need to align multiple layers of arrayed components during assembly of the above-mentioned imaging systems gives them no advantage over fish eye lenses. For practical implementations of compound eyes with wide FOV, the requirement of curvature-compatible, self-aligned fabrications schemes is evident.

In this work, biologically inspired artificial compound eyes were developed in a small form factor with three-dimensional (3D) configurations. These biomimetic compound eyes are anatomically as well as functionally close to natural compound eyes (Fig. 1C). The artificial ommatidium consists of a honeycomb-packed hexagonal microlens with a low Fresnel number (N_F < 10), a cuvette-shaped polymer cone, and a polymer waveguide that has a higher index solid core surrounded by a lower index solid cladding in the polymer resin (Fig. 1D). Three-dimensional polymer synthesis of an artificial compound eye can be realized through microlens templating, reconfigurable microtemplating, and self-writing in a photosensitive polymer resin. Each ommatidium was omnidirectionally arranged in a hemispherical polymer dome. Like the crystalline cone in nature, the polymer cone helps guide the focused light into the polymer waveguide, and subsequently the guided light arrives at the end of the waveguide core (*12*). Lastly, light detection can be done by photodetector arrays. In 3D implementation, microlens-assisted self-writing and polymer replication processes were used to minimize the lens-waveguide coupling loss and to realize a spherical configuration, respectively.

Polymer synthesis of artificial ommatidia can be done by using a microlens-assisted self-writing of waveguides and two cross-linking mechanisms in a photosensitive polymer resin (*13*) (Fig. 2A). Ultraviolet (UV) light was focused through low N_F microlenses molded by a photosensitive polymer resin and was self-trapped after passing the focal

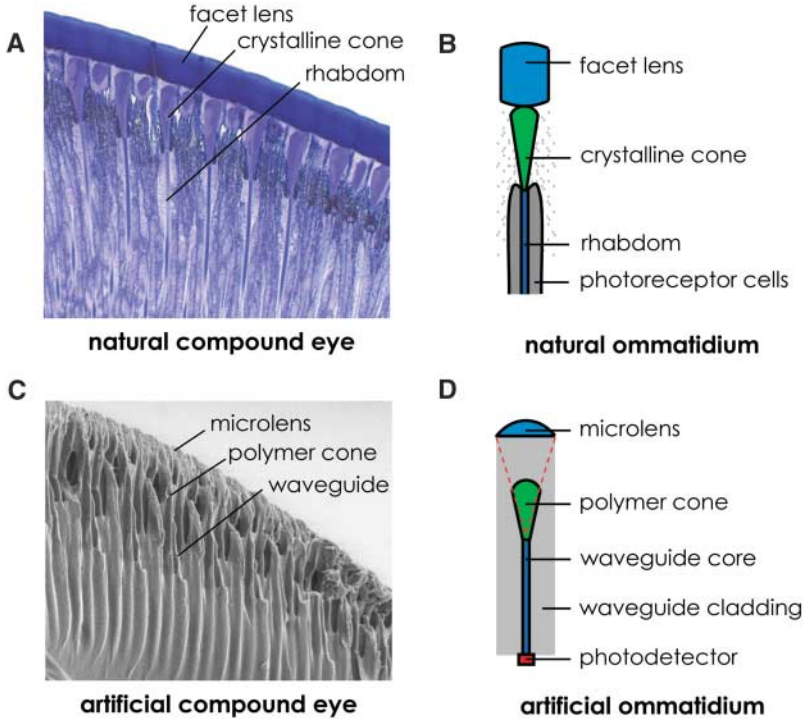

Fig. 1. Anatomical comparisons between a natural compound eye and an artificial compound eye described from the cross sections. (**A**) An optical micrograph of a honeybee's apposition compound eye (courtesy of B. Greiner). As an individual optical unit, (**B**) a natural ommatidium consists of a facet lens, a crystalline cone, and photoreceptor cells with a wave-guiding rhabdom. (**C**) A scanning electron micrograph of an artificial compound eye and (**D**) an artificial ommatidium comprising a microlens, a polymer cone, and an optical waveguide that has a higher index core surrounded by a lower index cladding in a polymer resin. Light impinging onto a microlens is coupled with polymer cones and waveguides and then guided to the end of the waveguide.

Biomolecular Nanotechnology Center, Berkeley Sensor and Actuator Center, Department of Bioengineering, 485 Evans Hall No. 1762, University of California, Berkeley, CA 94720, USA.

*To whom correspondence should be addressed. E-mail: lplee@socrates.berkeley.edu

plane because of the refractive index change by the photopolymerization (*14–18*).

The exposed portion above threshold energy for photopolymerization was photocross-linked by postbaking. The underexposed portion below threshold energy was still UV sensitive but was thermally cross-linked by heating above the temperature where a photoacid generator (PAG) in the photosensitive polymer resin starts to degrade. At that point, the unexposed portion became insensitive to additional UV light. In the experiment, a commercialized negative tone photoresist (SU-8, Microchem Corporation, Newton, MA) was used as a photosensitive polymer resin. Initially the refractive index of an SU-8 monomer in a liquid phase, measured by an Abbe refractometer (ARIAS 500, Reichert, Incorporated, Depew, NY), was $n_{monomer}$ = 1.550. The index of a 1.5-μm-thick thin monomer film, prepared by spincoating and a soft bake, increased to 1.584 because of the evaporation of SU-8 solvent, that is, gamma butyrolactone (GBL). After UV exposure of 900 mJ/cm^2 and a postexposure bake, the index change measured by a spectroscopic ellipsometer increases up to Δn_{photo} = 0.021, and the fully photocross-linked SU-8 index was n_{photo} = 1.605. After thermal cross-linking, the index of the exposed portion fully cross-linked by UV was constant, but that of the unexposed portion decreased by 0.008. Consequently, the maximum index change between both cross-linking core and cladding eventually turned out to be $\Delta n_{SU\text{-}8}$ = 0.029.

The formation of the self-written waveguide during UV exposure was simulated by using a fast Fourier transform–based beam propagation method (Fig. 2B). In the simulation, the propagating exposure beam, while being diffracted by the index distribution, imparts photon energy to the photosensitive medium and modifies its refractive index as well. The modified refractive index profile was used to simulate the next round of propagation, and so on. The imparted energy, or the irradiation dose, E, at one location has been calculated as the product of the field intensity at that point and the unit time duration. The increase in the refractive index is approximated to be linear between the initial and the saturated indices. The microlens first focuses the exposure beam with about 50 μm of back focal length. The initial beam intensity and the unit time duration have been iteratively optimized to initiate the self-writing process from the focal point. The relatively large refractive index contrast of the photosensitive resin facilitated the formation of a straight, over-100-μm-long waveguide. The "diffusion" of the refractive index due to the chemically amplifying nature of the photosensitive resin (SU-8) was ignored in this simulation. As a result, the simulated waveguide was thinner than the one obtained experimentally. The rough surface of the simulated waveguide, in contrast to the smooth surface of the actual self-written waveguides, can also be ascribed to the exclusion of the diffusion effect. The combined action of the high index contrast and the diffusive, self-smoothing index profile was required to improve the efficiency of the self-writing process. Other than that, the simulated index profiles taken when E reaches 5 to 20 times the value of the cross-linking threshold, E_{th}, exhibited good qualitative agreements with the observed waveguide structures. In our experiment, with the use of the previous method, the formation of large-scale artificial ommatidia self-written by 300-μm microlenses depended on UV exposure energy. It turned out that the formation of a polymer cone occurs after that of a waveguide core as UV exposure energy increases (Fig. 2C). At the level of hexagonal microlens of 25 μm in diameter, the formation of polymer cones and waveguide cores was also visualized by dark-field optical microscopy (Fig. 2D). The visualization was accomplished by dissolving unexposed portions in a solvent before thermal cross-linking. Polymer cones and waveguide cores were placed on a substrate because of the high aspect ratio of core diameter to core length.

The light guiding (λ = 635 nm) through artificial ommatidia has also been demonstrated by optical sectioning along the optical axis with a laser scanning transmission confocal microscope. An artificial ommatidium after thermal cross-linking (microlens with F number of 1.93 (F/1.93), lens diameter of 30 μm (D_L = 30 μm), and N_F = 7.3; index difference between waveguide core and cladding was 0.029) showed

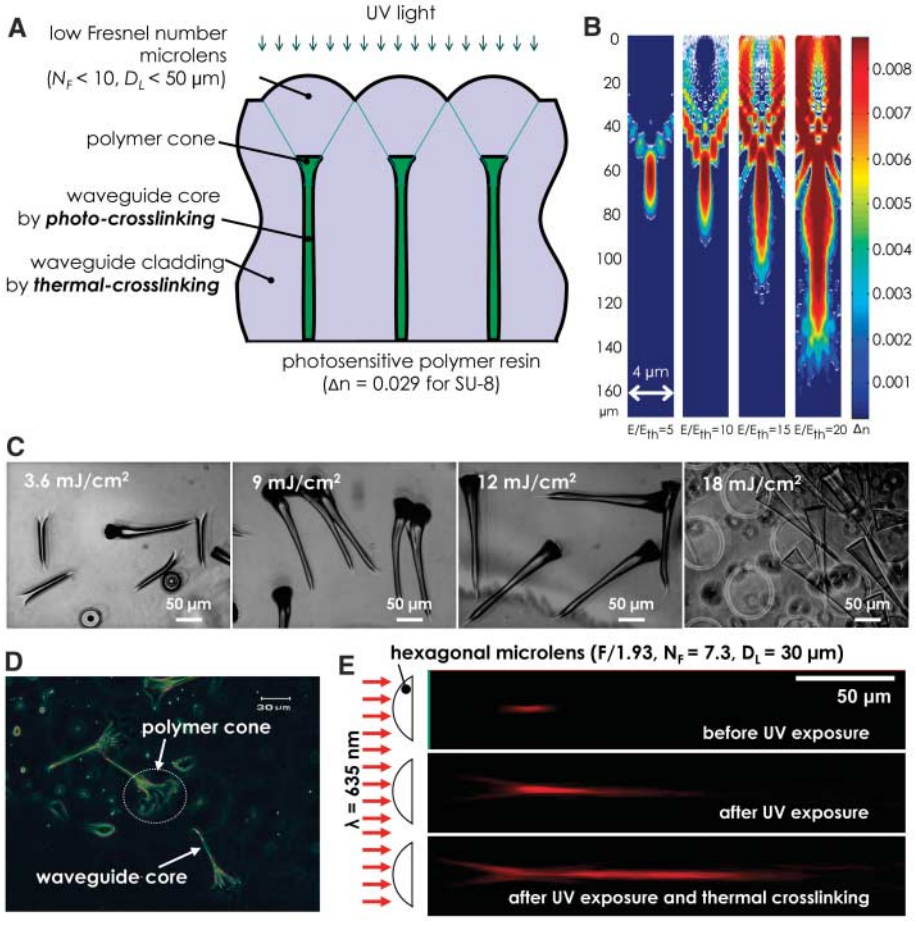

Fig. 2. Polymer synthesis of artificial ommatidia. (**A**) Two-step cross-linking mechanisms, that is, photocross-linking for waveguide cores and thermal cross-linking for waveguide claddings. (**B**) Simulated refractive index distributions of polymer waveguides formed by microlens-assisted self-writing by four different values of E. E_{th} is the threshold irradiation dose that can initiate the cross-linking process in the polymer. (**C**) The formation of polymer cones and waveguide cores self-written by 300-μm-diameter microlenses depending on UV exposure. (**D**) A dark-field micrograph of polymer cones and waveguide cores placed on a substrate after completely dissolving unexposed portions in a solvent before thermal cross-linking. Note that the waveguide cores fall down because of the high aspect ratio of core diameter to core length. (**E**) Optically sectioned confocal micrographs of light at 635 nm coupled through an artificial ommatidium before UV exposure (only microlens), after UV exposure (waveguide core by photocross-linking), and after UV exposure and thermal cross-linking.

strong light guiding in comparison with only a microlens or with only UV photopolymerization (Fig. 2E).

The spherical configuration of artificial ommatidia can be achieved through a polymer replication process by reconfigurable microtemplating, that is, the polymer replication using the deformed elastomer membrane with microlens patterns (*19*) and self-written waveguides with a lens-assisted UV exposure for self-written waveguides. Honeycomb-packed hexagonal photoresist microlens arrays were prepared on a silicon substrate (Fig. 3A), and the lens template was molded onto a 22-μm-thick slab of polydimethylsiloxane (PDMS) elastomer (Fig. 3B). For reconfigurable microtemplating, a 5-mm-thick PDMS elastomer slab with a microfluidic channel and a circular through-hole 2.5 mm in diameter perforated by mechanical punching was permanently bonded to a 22-μm-thick PDMS replica of concave microlenses after an oxygen plasma surface treatment. The microlens replica was then released from the microlens template (Fig. 3C). Negative air pressure ranging from 5 to 30 kPa was applied through a microfluidic channel to deform the PDMS membrane with concave microlenses (Fig. 3D). A solvent-free UV-curable epoxy resin (NOA 68, Norland Products Incorporated, Cranbury, NJ) was precisely dispensed onto the deformed elastomer membrane, covered with a glass coverslip, and then fully cross-linked for 2 hours with UV light of 0.5 mW/cm^2 (Fig. 3E). For a batch replication, a 3D master mold was prepared with a five-by-five array of the 3D epoxy resin replicas with different curvatures glued on a Petri dish, and the master mold was again replicated with PDMS (Fig. 3F). The pattern polarity of the 3D PDMS replica was reversed by molding it with a commercial photosensitive polymer resin (NANO SU-8, formulated in cyclopentanone). The volume of 40 μl was precisely dispensed in each concave dome and prebaked at 120°C for 20 min to remove the solvent. An additional prebake process was also carried out at 120°C for 1 hour right after covering each droplet with a 10-mm-diameter circular glass (Fig. 3G). The SU-8 replica with convex microlenses along the circumference kept its shape up to 120°C because the glass transition temperature of SU-8 increases with the soft-bake temperature (*20*). However, the microlens patterns on an SU-8 droplet may disappear with an insufficient prebake. In particular, the release of the SU-8 replica needs to be carried out at room temperature; otherwise, the gel-like SU-8 may not completely release from the PDMS mold. Next, a partially coherent UV light source from a photolithographic tool (Q4000 MA, Quintel Corporation, Morgan Hill, CA; 12 mW/cm^2 at 365 nm) was used to form a polymer cone and a waveguide under each microlens. The spherical arrangement of artificial ommatidia was determined by the spherical illumination of UV light, which can be achieved with a spherical mirror or a high numerical aperture (*NA*) condenser lens. In the experiment, an aspheric condenser lens (lens diameter of 23 mm, *F*/0.5, and back focal length of 6.9 mm) was chosen for ease of use in the experiment even though the angular span was limited by the *NA* of the condenser lens (Fig. 3H). For instance, the illumination angle for *F*/0.3 is ±45°. However, a spherical mirror-assisted illumination is recommended for UV illumination with a wide angle. The spherically UV-exposed SU-8 replica was then postexposure baked (at 90°C for 15 min) for photocross-linking and finally hard baked (at 150°C for 3 hours) for thermal cross-linking. Two scanning electron microscope (SEM) images showed that honeycomb-packed hexagonal microlenses of about 8370 (*F*/2.2, 25 μm in diagonal) are spherically arranged on a hemispherical polymer dome 2.5 mm in diameter (Fig. 3, I and J). Under the microlenses, self-aligned polymer cones and waveguide cores as well as cladding were observed by a cross-sectional SEM image (Fig. 3K).

Light from point light sources at infinity was coupled into the omnidirectionally arranged ommatidia with different coupling efficiency because each ommatidium covered a different direction. Consequently, the angular sensitivity function (ASF) of a single ommatidium can be reconstructed by measuring the relative intensity of the light at the distal end of each ommatidium, as proposed in a previous work (*21*). However, the actual measurement had not been carried out yet. The ASF of a single ommatidium in an artificial compound eye was measured by performing 3D optical sectioning based on laser scanning confocal microscopy (Fig. 4A). The optical sectioning of the artificial compound eye was carried out under normally incident light at 532 nm with a transmission confocal microscope (Zeiss 510, Carl Zeiss MicroImaging, Incorporated, Thornwood, NY) (Fig. 4B). Starting from the apex of the artificial compound eye, the vertical scanning was performed

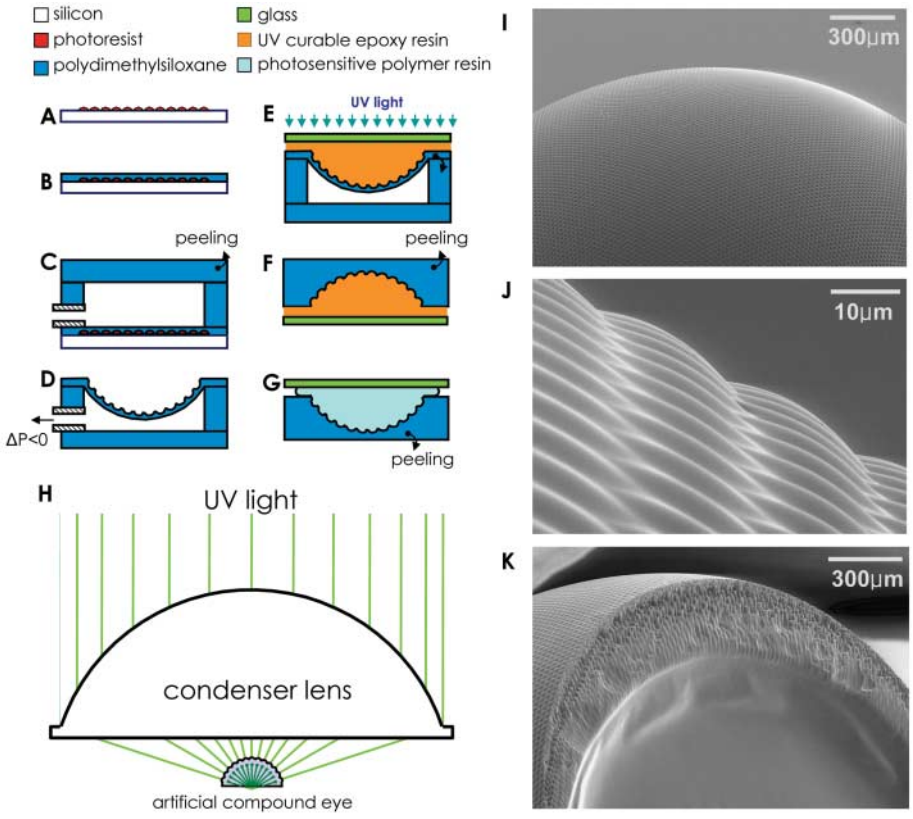

Fig. 3. The 3D polymer synthesis of biomimetic artificial compound eyes using (**A**) a honeycomb-packed polymer microlens process, (**B** to **G**) a reconfigurable microtemplating polymer process, and (**H**) a self-written waveguide process in photosensitive polymer resin by lens-assisted radial UV exposure. (A) Microlens template by a resist reflow method, (B) first PDMS molding, (C) PDMS bonding, (D) PDMS membrane deformation, (E) replication with UV curable polymer resin, (F) second PDMS molding, (G) photosensitive polymer resin (SU-8) molding, and (H) lens-assisted radial UV exposure and thermal cross-linking for self-written waveguides. SEM images of an artificial compound eye. (**I**) Spherical arrangement of 8370 artificial ommatidia on a hemispherical polymer dome 2.5 mm in diameter, (**J**) hexagonal microlenses, and (**K**) a cross section with the spherical arrangement of artificial ommatidia consisting of microlenses, polymer cones, and waveguide arrays.

over a range of 200 μm with a 2-μm increment. At each vertical increment, a 765-μm–by–765-μm area perpendicular to the incident light was laterally scanned with a 0.8-μm resolution. The confocal image on the *xy* plane was taken at 80 μm below the apex of the artificial compound eye. The cross-sectional confocal images scanned along the lines *aa′* and *bb′* are also shown at the top and right sides of the main image, respectively. The distributions of the relative output intensity measured along the two lines at the vertical position are also included on the bottom and left sides, respectively. The relative intensity of each peak represents the sensitivity of an individual ommatidium to different incidence angles. The observed distributions of relative intensity in *x* and *y* directions are slightly asymmetric because of the honeycomb packing of hexagonal microlenses.

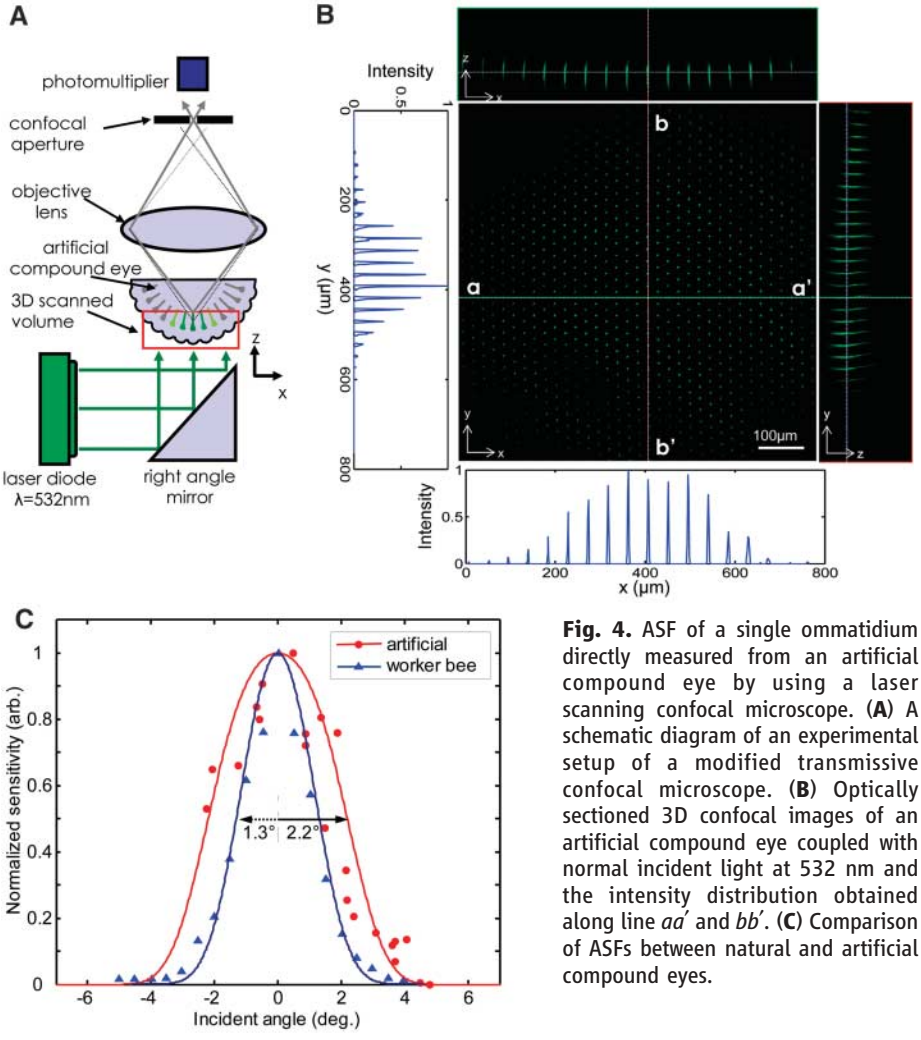

Fig. 4. ASF of a single ommatidium directly measured from an artificial compound eye by using a laser scanning confocal microscope. (**A**) A schematic diagram of an experimental setup of a modified transmissive confocal microscope. (**B**) Optically sectioned 3D confocal images of an artificial compound eye coupled with normal incident light at 532 nm and the intensity distribution obtained along line *aa′* and *bb′*. (**C**) Comparison of ASFs between natural and artificial compound eyes.

Table 1. Comparisons between artificial and natural compound eyes.

	Artificial eyes	Natural eyes (bees)	Ref.
Shape of lens aperture	Hexagon	Hexagon	(*22*)
Maximal lens diameter	25 μm	20∼36 μm	(*22*)
F number	1.8∼2.9	2.7∼3.3	(*22*)
N_F at 635 nm	3.4∼5.5	2.4∼5.3	
Number of lenses	8370	3421∼4883	(*22*)
Refractive index of lens	1.584	1.363	(*12*)
Index difference (core/cladding)	0.029 (1.614/1.584)	0.023 (1.363/1.340)	(*25*)
Waveguide shape	Cylindrical	Cylindrical	(*22*)
Waveguide core	5.1∼6.3 μm	2∼8 μm	(*22*)
Waveguide length	150∼300 μm	220∼350 μm	(*22*)
ASF	1.1°∼4.4°	1.6°∼4.7°	(*22*, *23*)

To obtain the ASF of a single ommatidium, we first measured the orientation of each waveguide from the vertically scanned confocal images. The relative intensity distribution was plotted with respect to the incidence angle (Fig. 4C). Because of the tilting of the artificial ommatidium under confocal scanning, the measurement on the left-hand side was not complete. If a general symmetry is assumed, the acceptance angle, or the full width at half maximum of the measured ASF, is 4.4°. The value is comparable to those of natural compound eyes, which range from 1.6° to 4.7° (*22*). As shown in the superimposed curve, the acceptance angle of a worker bee ommatidium is ∼2.5° (*23*). We also reconstructed the theoretical ASFs by using the lens-waveguide coupling model proposed by Stavenga (*12*). The model takes both the diffraction by microscale lenses and the excitation of waveguide modes by the diffraction image into consideration. The results of reconstruction using only the fundamental waveguide mode were superimposed in Fig. 4C. We used the optical and structural parameters of the worker bee reported by Laughlin and Horridge (*23*) and Snyder and Pask (*24*). We point out that the use of only the fundamental mode of cylindrical waveguides for the reconstruction led to the best fit with experimental data for both cases. Although the approximation may be acceptable for waveguides in worker bee ommatidia, which support only two modes, it may not be applicable to the waveguides of artificial ommatidia, which support more than 10 modes. The unexpected agreement between the measured ASF and the single-mode approximated reconstruction suggests that the index distribution of the self-written waveguides deviates from the step profile and hence degrades the model. The current artificial ommatidium exhibits an acceptance angle wider than the interommatidial angle (∼1.5°), and it will suffer from overlap-induced image degradation. The main reason is that the curvature of the eyelet is increased by the large deformation of a polymer membrane during the polymer replication process. However, this problem can be resolved by controlling the local distribution of the microlenses. The optical sectioning technique not only enabled the visualization of the light propagation through microlenses but also facilitated the precise measurement of beam spot sizes at the focal plane of the microlenses and waveguide cores, waveguide modes, coupling loss, waveguide length, and most importantly the angular acceptance. More optical measurement results were comparable with the previously measured characteristics of the bee (Table 1). Our results show that both the physical dimensions and the optical characteristics of our artificial ommatidia are very comparable to those found in nature. Therefore, this 3D polymer fabrication method of biologically inspired optical systems has potential for a

broad range of optical applications, such as data storage and readout, medical diagnostics, surveillance imaging, and light-field photography.

References and Notes

1. J. H. van Hateren, in *Facets of Vision*, D. G. Stavenga, R. C. Hardie, Eds. (Springer-Verlag, Berlin, 1989), pp. 74–89.
2. M. F. Land, *Annu. Rev. Entomol.* **42**, 147 (1997).
3. D. G. Stavenga, J. H. van Hateren, *J. Opt. Soc. Am. A* **8**, 14 (1991).
4. A. W. Snyder, in *Comparative Physiology and Evolution of Vision in Invertebrates A: Invertebrate Photorecepters*, H. Autum, Ed. (Springer-Verlag, Berlin, 1979), pp. 225–314.
5. R. C. Hardie, in *Progress in Sensory Physiology*, D. Ottoson, Ed. (Springer-Verlag, Berlin, 1985), pp. 1–79.
6. R. C. Hardie, K. Vogt, A. Rudolph, *J. Insect Physiol.* **35**, 423 (1989).
7. J. Tanida *et al.*, *Appl. Opt.* **40**, 1806 (2001).
8. J. Duparre, P. Dannberg, P. Schreiber, A. Brauer, A. Tunnermann, *Appl. Opt.* **44**, 2949 (2005).
9. S. Ogata, J. Ishida, T. Sasano, *Opt. Eng.* **33**, 3649 (1994).
10. K. Hamanaka *et al.*, *Opt. Rev.* **3**, 264 (1996).
11. L. P. Lee, R. Szema, *Science* **310**, 1148 (2005).
12. D. G. Stavenga, *J. Comp. Physiol. A* **189**, 1 (2003).
13. J. Kim, K. Jeong, L. P. Lee, *Opt. Lett.* **30**, 5 (2005).
14. A. S. Kewitsch, A. Yariv, *Opt. Lett.* **21**, 24 (1996).
15. M. Kagami, T. Yamashita, H. Lto, *Appl. Phys. Lett.* **79**, 1079 (2001).
16. S. Shoji, S. Kawata, A. Sukhorukov, Y. S. Kivashar, *Opt. Lett.* **27**, 185 (2002).
17. U. Streppel, P. Dannberg, C. Wachter, A. Brauer, R. Kowarschik, *Appl. Opt.* **42**, 3570 (2003).
18. T. Yamashita *et al.*, *IEEE Photonics Technol. Lett.* **16**, 801 (2004).
19. Y. Xia *et al.*, *Science* **273**, 347 (1996).
20. R. Feng, R. J. Farris, *J. Micromechanics Microengineering* **13**, 80 (2003).
21. J. S. Sanders, C. E. Halford, *Opt. Eng.* **34**, 222 (1995).
22. B. Greiner, W. A. Ribi, E. J. Warrant, *Cell Tissue Res.* **316**, 377 (2004).
23. S. B. Laughlin, G. A. Horridge, *J. Comp. Physiol. A* **74**, 329 (1971).
24. A. W. Snyder, C. Pask, *J. Comp. Physiol. A* **80**, 51 (1972).
25. D. G. Beersma, B. J. Hoenders, A. M. Huiser, P. V. Toorn, *J. Opt. Soc. Am.* **72**, 583 (1982).

26. We acknowledge B. Greiner at Dalhousie University, Halifax, Nova Scotia, Canada, for helpful discussion and for the micrograph in Fig. 1A. and all staff at Biological Imaging Facility (BIF) and Microfabrication Laboratory (MicroLab) of the University of California at Berkeley for their support. This work is supported by the Defense Science Office of Defense Advanced Research Project Agency.

28 November 2005; accepted 23 March 2006
10.1126/science.1123053

A Population of Comets in the Main Asteroid Belt

Henry H. Hsieh* and David Jewitt

Comets are icy bodies that sublimate and become active when close to the Sun. They are believed to originate in two cold reservoirs beyond the orbit of Neptune: the Kuiper Belt (equilibrium temperatures of ~40 kelvin) and the Oort Cloud (~10 kelvin). We present optical data showing the existence of a population of comets originating in a third reservoir: the main asteroid belt. The main-belt comets are unlike the Kuiper Belt and Oort Cloud comets in that they likely formed where they currently reside and may be collisionally activated. The existence of the main-belt comets lends new support to the idea that main-belt objects could be a major source of terrestrial water.

Temperatures in the outer parts of the protoplanetary disk of the Sun, beyond a critical distance known as the snow line (*1*), were low enough for water to condense as ice. The icy planetesimals that formed beyond the snow line are the progenitors of today's comets—ice-rich bodies that sublimate when close to the Sun, producing distinctive unbound atmospheres ("comae") and tails (*2*). The active lifetimes [$\sim 10^4$ years (*3*)] of comets that pass inside Jupiter's orbit are short relative to the age of the solar system (4.6×10^9 years). This means that currently active comets must have only recently arrived in the inner solar system from cold reservoirs elsewhere, otherwise they would have exhausted their volatile material long ago. Two such originating reservoirs are well established. The Kuiper Belt (*4*) beyond Neptune (~30 to 50 AU from the Sun) supplies the so-called Jupiter-family comets (JFCs), whereas the much more distant Oort Cloud (*5*) (~3000 to 50,000 AU) supplies the Halley-family and long-period comets (*3*, *6*).

Although the dominant cometary reservoirs are located beyond the orbit of Neptune, the main cometary volatile, water, is stable as ice down to much smaller heliocentric distances (*7*), and it has long been suspected that other populations (such as the Hilda asteroids at 4 AU and the jovian Trojans at 5 AU) might be ice-rich, dormant comets (*8*, *9*). However, the active comet population we see today consists mainly of objects from the Kuiper Belt and Oort Cloud that have been scattered onto Jupiter-crossing orbits by gravitational interactions with the giant planets (*3*, *10*). Even the dynamically peculiar comet 2P/Encke is believed to have originated in the Kuiper Belt, albeit with an orbital evolutionary history strongly influenced by nongravitational forces induced by cometary outgassing (*11*, *12*).

Despite occupying a thoroughly asteroidal orbit in the main belt between the orbits of Mars and Jupiter, asteroid 7968 Elst-Pizarro (also known as comet 133P/Elst-Pizarro) was observed to eject dust like a comet when near perihelion in both 1996 and 2002 (*13*, *14*).

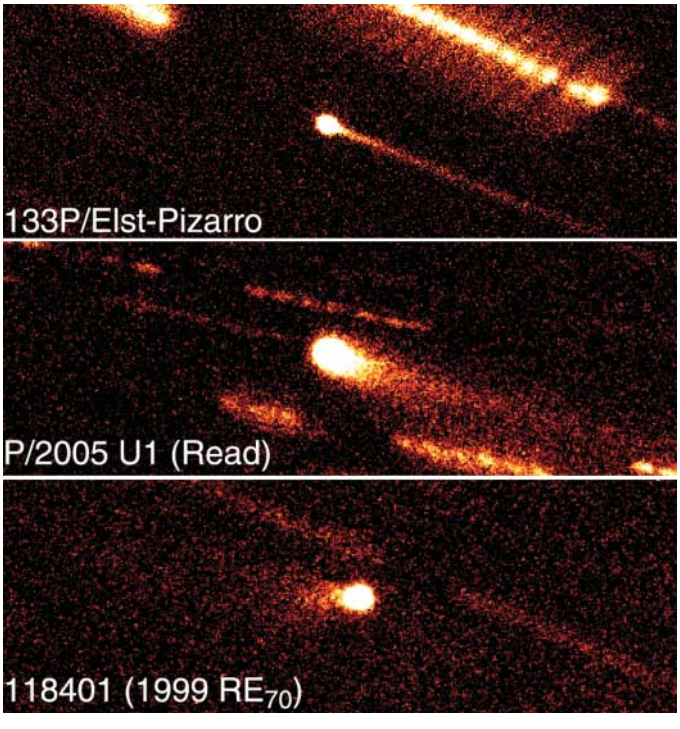

Fig. 1. *R*-band (wavelength 0.65 μm) images of MBCs 133P/Elst-Pizarro on 7 September 2002 (*14*), P/2005 U1 (Read) on 10 November 2005, and 118401 (1999 RE_{70}) on 27 December 2005 (all dates UT). All images are composites (0.5′ by 1.5′ in size, with north at the top and east to the left) from data taken at the University of Hawaii 2.2-m telescope on Mauna Kea, and represent 1.1 hours, 1.9 hours, and 2.8 hours of total effective exposure time, respectively. Streaked objects in each panel are background stars and galaxies that have been trailed by the nonsidereal motions of the comets. Geometric circumstances of these observations are given in Table 1.

Institute for Astronomy, University of Hawaii, 2680 Woodlawn Drive, Honolulu, HI 96822, USA.

*To whom correspondence should be addressed. E-mail: hsieh@ifa.hawaii.edu